Journal of Materials Chemistry A

Li-ion and Na-ion intercalation in layered MnO_2 cathodes enabled by using bismuth as a cation pillar

Journal:	*Journal of Materials Chemistry A*
Manuscript ID	TA-ART-02-2023-000684.R1
Article Type:	Paper
Date Submitted by the Author:	15-Apr-2023
Complete List of Authors:	Kim, Matthew; Northeastern University, Chemical Engineering Zimmerer, Eric; Northeastern University, Chemical Engineering Piontkowski, Zachary ; Sandia National Laboratories, Department of Applied Optical and Plasma Science Rodriguez, Mark; Sandia National Laboratories, Schorr, Noah; Sandia National Laboratories Wygant, Bryan; Sandia National Laboratories, Department of Photovoltaics and Materials Technology Okasinski, John; Argonne National Laboratory, Advanced Photon Source X-ray Sciences Division Chuang, Andrew; Argonne National Laboratory, X-ray Sciences Division Lambert, Timothy; Sandia National Laboratories, Materials, Devices & Energy Technologies Gallaway, Joshua; Northeastern University, Chemical Engineering

Li-ion and Na-ion intercalation in layered MnO_2 cathodes enabled by using bismuth as a cation pillar

Matthew A. Kim [1], Eric K. Zimmerer [1], Zachary T. Piontkowski [2], Mark A. Rodriguez [3], Noah B. Schorr [4], Bryan R. Wygant [4], John S. Okasinski [5], Andrew C. Chuang [5], Timothy N. Lambert [4], and Joshua W. Gallaway *, [1]

1. Department of Chemical Engineering, Northeastern University, 360 Huntington Avenue, Boston, MA 02115, USA.

2. Department of Applied Optical and Plasma Science, Sandia National Laboratories, Albuquerque, New Mexico 87185, USA

3. Materials Characterization and Performance Department, Sandia National Laboratories, Albuquerque, New Mexico 87185, USA

4. Department of Photovoltaics and Materials Technology, Sandia National Laboratories; Albuquerque, New Mexico, USA, 87185, USA.

5. X-ray Science Division, Advanced Photon Source, Argonne National Laboratory, Lemont, Illinois 60439, USA.

* Corresponding author, j.gallaway@northeastern.edu

Abstract

Low-cost batteries based on Earth-abundant materials are needed for large-scale electrical storage for the grid. Cathodes based almost entirely on Mn oxides would reduce overall battery cost but cycling of Mn oxides is often not stable. In Li-ion cells, most polymorphs of MnO_2 undergo irreversible transformation to spinel $LiMn_2O_4$ during cycling, causing capacity loss. Doping MnO_2 with Bi is known to stabilize the structure, but previous reports have relied on low-crystallinity material making it impossible to pinpoint the Bi location in the structure or its mechanism. Herein, we report a series of hydrated Bi-doped layered MnO_2 compounds and characterize their structures as a function of Bi amount. Bi is shown to reside in the material interlayer, provoking higher long-range structural order even at a low doping level of 1.3%. Doped material improves the specific capacity and stability of cycling in both Li-ion and Na-ion cells. A high level of Bi doping, 4.3%, causes loss of the interlayer crystal water in non-aqueous electrolyte, and this reduces the interlayer distance. Crystal water is shown to be beneficial in a Na-ion system, while its loss improves Li-ion cycling. This provides fundamental insight into how pillaring by a heavy, multivalent cation stabilizes layered oxides.

1. Introduction

Li-ion batteries enable almost all modern portable electronics and electric vehicles. However, for electrification of sectors that are more cost-sensitive, such as grid-scale batteries to balance renewables, Li-ion battery materials require further evolution. This is because their cost is too high, and the largest cost in most cells is the cathode. Many cathode active materials are based on transition metal oxides containing Co and Ni, which contribute significantly to the cost. For decades it has been understood that cathodes based almost entirely on Mn oxides would enable lower-cost energy storage applications.[1] The large volume of batteries that will be required to integrate storage throughout the power grid will require cathode materials based on more Earth-abundant elements, but also may require a more Earth-abundant working ion, like Na^+ in Na-ion batteries, or H^+/OH^- in aqueous batteries.[2, 3]

From a cost and sustainability perspective MnO_2 is an ideal cathode material for batteries. There are a complex array of polymorphs of MnO_2, and one type, electrolytic manganese dioxide (EMD), is a high-volume production material used extensively in the primary battery industry.[4] Li-ion batteries using a spinel $LiMn_2O_4$ cathode (lithium manganese oxide or LMO) are used commercially, but have low capacity (~100 mAh/g) and suffer from instability due to Mn dissolution.[5] Many types of lithiated MnO_2 compounds have been studied as potential cathodes, such as orthorhombic $LiMnO_2$, layered monoclinic $LiMnO_2$, and tetragonal $LiMnO_2$.[6-9] However, during cycling these all transform to the spinel $LiMn_2O_4$ and therefore fall greatly in cyclable capacity.[7, 10] Various strategies have been reported to prevent a Li-containing layered MnO_2 from conversion to the undesired $LiMn_2O_4$ spinel during cycling.[11-14] For example, beginning with an O2 oxygen lattice (instead of O3) as reported by Paulsen et al.[15] Because an O3 structure is very similar to the oxygen lattice in spinel, the undesired conversion is more likely to occur, and an O2 lattice prevents this. Li-rich materials such as Li_2MnO_3 have also been studied extensively.[16] In all of these cases, the stated

or implicit goal has been a cathode material that is a general analog to $LiCoO_2$, with most of the capacity in a voltage range of 3-4 V vs Li and a capacity near 200 mAh/g.

Another type of layered MnO_2 are phyllomanganates or birnessite- and buserite-type materials.[17, 18] Phyllomanganates are layered structures made of slabs of edge-sharing MnO_6 units (**Fig 1a**), which often have some amount of Mn vacancies. The Mn can be 4+ or 3+, and any net negative charge due to vacancies or Mn^{3+} occupancy is balanced by cations in the interlayer between the slabs (**Fig 1b**). Common interlayer ions are Na^+ and K^+, but an extensive number have been reported.[19] Structural or crystal water is also found in the interlayer. Material with a single layer of water has an interlayer distance of ~7 Å and is called birnessite or δ-MnO_2. A double layer of water results in ~10 Å, called buserite.

Phyllomanganates cycled with Li in dry, non-aqueous electrolyte also undergo conversion to spinel $LiMn_2O_4$.[20] Chen and Whittingham compared the Li cycling of dehydrated phyllomanganates with different interlayer cations: Li, Na, and K.[21] The K-inserted MnO_2 had the best capacity retention, and this was ascribed to a larger interlayer distance (4.86, 5.61, and 6.44 Å for Li, Na, and K). The larger interlayer was less favorable to accommodating Mn^{2+} during the conversion to spinel $LiMn_2O_4$, thus mitigating the often-problematic failure mechanism. This finding demonstrates that the interlayer species have a strong effect on cycling performance. Recently, there have been several reports using phyllomanganate cathode materials in dry, non-aqueous electrolyte with the interlayer crystal water intact.[22-24] Since the crystal water is the species that defines the interlayer distance, it may be a critical component during cycling. The presence of structural water has been shown to improve Li^+ insertion kinetics, in a study by Mitchell and co-workers, which compared WO_3 and $WO_3 \cdot H_2O$ in non-aqueous electrolyte.[25]

Bi has often been reported as a modifying or doping element with MnO_2. This stems from the fact that Bi modification imparts two-electron rechargeability (~617 mAh/g) to MnO_2 in aqueous alkaline electrolyte.[26] However, the mechanism by which Bi does this is debated in the literature, with no clear explanation agreed upon. The rechargeable alkaline Bi-MnO_2 cathode involves proton insertion followed by an electrochemical

conversion to $Mn(OH)_2$, and the transition period between these involves multiple phenomena and is complex to study.[27]

In terms of modification of MnO_2, Bi is often referred to as a cation pillar.[28] The concept is that a cation in the interlayer pins the slabs into place, providing stability. However, the molecular phenomenon that leads to this pillaring varies in explanation. It has been recognized that Bi pillaring could increase stability of Li-ion cathodes based on MnO_2.[29] Bach and co-workers previously reported using Bi-pillared MnO_2 as a Li-ion intercalation host.[30] However, the material was poorly crystalline, and the Bi doping amounts were relatively large. Yang, et al. reported Bi-modified MnO_2 with stable cycling of 145 mAh/g in Li-ion cells.[31] This material was amorphous and remained so during cycling. Characterization of amorphous materials is challenging, so the source of stable cycling enabled by Bi remained unknown. Higher capacity is desired, as well as characterization of why Bi stabilizes (de)intercalation. Applying this approach to Na-ion batteries is also desired. This is needed to explore possible Li-ion and Na-ion cathodes for low-cost applications such as grid storage, as well as for fundamental understanding of how Bi interacts with Mn, where it is found in the crystal structure, and why it stabilizes or pillars the structure.

Our purpose in this study was two-fold. The first was to prepare a series of layered Bi-doped MnO_2 compounds and characterize these chemically, structurally, and morphologically as a function of Bi amount. This would provide insight into how Bi interacts with MnO_2 structurally. The second was to use these compounds to demonstrate the phenomenon of Bi-pillaring, in which structural changes of the intercalation host are prevented or minimized by the presence of Bi in the interlayer. This was done using Li-ion and Na-ion batteries. Of particular interest was the effect of Bi on other interlayer species, such as crystal water, which determines the interlayer spacing. Our findings demonstrate that doped Bi is substantially incorporated into the interlayer, where it causes increased structural ordering of the material. This result is supported by X-ray diffraction as well as Raman spectroscopy. Bi doping at a low level (1.3%) and a high level (4.3%) both improve cycling stability and specific capacity in Li-ion and Na-ion cells. Higher doping levels provoke loss of the crystal water when the cathode is wetted with the non-aqueous electrolyte, and this changes the interlayer distance. The optimum Bi amount for stable cycling is different for Li-ion and

Na-ion cases: high Bi doping and a smaller interlayer is better for Li cycling, while the low-doping case is better for Na cycling.

Experimental section

Synthesis of layered MnO_2 materials

For synthesis of K_x-MnO_2, a solid-state method reported by Kim *et al.* was used. It relied on the thermal decomposition of $KMnO_4$ at 800 °C in flowing air for 5 hours followed by washing with DI water.[32] $KMnO_4$ (Sigma-Aldrich, ≥99.0%) was ground using an SPEX SamplePrep 8000 MIXER/MILL using a stainless-steel container and stainless-steel milling media and transferred to a ceramic boat. This was placed in a tube furnace with a flow of air. Temperature was ramped at 1 °C/min to 800 °C and held for 500 minutes. The temperature was allowed to cool to ambient while maintaining the flow of air. The product was ground and washed in DI water and then filter vacuumed. The obtained brown product was dried for 24 hours in a vacuum at 85 °C. Following this the material was kept in a desiccator until use.

For synthesis of Bi-doped K_xBi_y-MnO_2, $KMnO_4$ and $Bi(NO_3)_3$ (Sigma-Aldrich, ≥99.99%) were ground in a mortar and pestle and put in a ceramic boat. The molar ratio of these materials was varied to obtain different levels of Bi doping. This was placed in a tube furnace with a flow of air. The temperature was ramped at 1 °C/min to 900 °C and held for 900 minutes. All remaining conditions were the same as with Bi-free material.

Materials characterization

Morphology and particle size were determined using scanning electron microscopy (SEM). A Thermofisher Scios Dualbeam SEM/FIB was used. Transmission electron microscopy was done using a Thermofisher Titan Themis 300 S/TEM. Materials were mounted on a carbon TEM grid after suspension in isopropyl alcohol. The values x and y in K_xBi_y-$MnO_2 \cdot nH_2O$ were determined from ICP-AES, conducted by Huffman Hazen Laboratories. Thermogravimetric analysis was used to determine the water content n. A 50-60 mg

sample of material were tested using a SDT Q600 V20.9 Build-20 instrument with temperature ramped at 10 °C/min under a flow of argon.

Electronic resistance was determined by 4-point probe. First powders were pressed into pellets. Approximately 100 mg of sample was placed between 13 mm diameter anvils of a Pike Technologies die press then pressed to 3500 pounds with a Carver press. Resulting pellets were then weighed, and the thickness measured via micrometer. The sheet resistance (Ω/sq) of each pellet was calculated from measuring the current and voltage measured by a Signatone 4-point probe (probe tip spacing 0.625 in, osmium tip 0.005 in diameter) in contact with the surface of the pellet. The contact of the probe to the pellet was done in a fashion to maintain the integrity of the surface (no cracking) while ensuring the probe was lowered evenly. Three spots on each pellet were measured for an average and standard deviation value of the resistivity. Using the thickness of each pellet the resistivity (Ω-cm) for each sample was calculated and converted to conductivity for reporting.

X-ray absorption spectroscopy (XAS) was performed at beamline 7-BM (QAS) of the National Synchrotron Light Source II (NSLS-II). Material was ground in a mortar and pestle and mounted between Kapton tape layers. X-ray energy was scanned across the Mn K-edge (6539 eV) in 5 eV steps. Data analysis was conducted in Athena. Linear combination fitting (LCF) was used to determine the bulk Mn oxidation state, using a series of Mn oxide standards.

Lab scale X-ray diffraction (XRD) was done using a Rigaku SmartLab X-ray powder diffractometer, at 0.002 degrees per step. High resolution X-ray powder diffraction was done at beamline 28-ID-2 (XPD) at NSLS-II. Samples were packed into Kapton tubes 3 mm in diameter and rotated as 2D measurements were collected at a wavelength of λ = 0.18766 Å. These 2D patterns were calibrated using LaB_6 and integrated in GSAS-II into a 1D pattern.

Raman spectroscopy was conducted using a Thermo Scientific DXR2xi Raman Imaging Microscope. Objective and magnification were a 50x confocal pinpoint. Grating groove density was 1200 gr/mm. Collection fiber core diameter was 200 μm. Raman shift axis was calibrated with a neon bulb. Light was unpolarized and collected in backscattering. Measurements were taken at 0.5 mW, at 2 second exposure times, for 50 scans (linescan) using a 455 nm laser. Settings were kept constant between samples

so that relative intensities could be comparable. For mapping autofocus between 400 cm^{-1} and 750 cm^{-1} was used at 1.0 mW for 20 scans.

Electrode preparation and cell assembly

The cathode slurry was prepared by combining active material and acetylene black conductive additive (MTI Corp) in a FlackTek DAC 150.1 FVZ-K SpeedMixer with n-methyl-2-pyrrolidone (NMP) solvent with dissolved polyvinylidene fluoride (PVDF) binder. The ratio of active material/carbon/PVDF binder was 70/20/10. The resulting slurry was applied to an Al foil (15 μm) with a doctor blade. The resulting cathode film was dried at 85 °C overnight to remove the NMP solvent. Slurries were applied at thicknesses between 60 and 90 μm wet thickness. After drying, cathodes were calendared to a thickness of 5 μm - 10 μm. Little variance in performance was found between the two cases. The areal loading was 1.5 - 2.5 mg/cm^2, and the areal capacity was 0.3-0.5 mAh/cm^2 based on a specific capacity of 200 mAh/g. The dried film was punched into disks 1.428 cm in diameter and transferred to an Ar atmosphere glovebox. In the antechamber they were dried under vacuum at 85 °C overnight.

CR2032 coin cells were used for electrochemical testing. Li-ion cells used 0.75 mm Li foil as the anode, 2 Celgard 2320 separators. The electrolyte was 1 M $LiPF_6$ in 70/30 ethylene carbonate and ethyl methyl carbonate (MTI Corp). Na-ion cells used Na foil as the anode and the same separators. The electrolyte was 1 M $NaPF_6$ in 50/50 ethylene carbonate and diethyl carbonate. Cells were crimped and then removed from the glovebox for testing. Cycling was galvanostatic at 25 mA/g for Li-ion and 45 mA/g for Na-ion, performed using an Arbin Instruments battery tester. Unlike traditional Li-ion batteries, these "empty host" cathodes began with a discharge step.[33]

Operando cell characterization

Small angle energy dispersive X-ray diffraction (EDXRD) was conducted at beamline 6-BM-A of the Advanced Photon Source (APS). This allowed diffraction data to be collected from within hermetically sealed 2032 coin cells. The incident white beam had an energy range of ~50–200 keV. The diffracted beam intensity was measured using a high-resolution germanium detector with a digital signal processor and an 8192-channel analyzer. The channel number to photon energy calibration was made by least squares fitting

to an LaB_6 standard. A small detector angle of 2θ = 1.5 degrees was used to probe changes in the large d-spacings characteristic of layered materials. The size of the EDXRD gauge volume was 10 μm, which matched well with the thickness of the cathode, ~15 μm. During operando experiments, the time of data collection for each point was 30 s. Diffraction data were smoothed using a Savitzky–Golay filter. Cells were cycled using a Maccor Battery Tester. Cycling current was 40 mA/g for both Li-ion and Na-ion cells.

Results and Discussion

Characterization of K_xBi_y-MnO_2 materials

Introduction of Bi^{3+} to δ-MnO_2 (**Fig 1b**) was accomplished during synthesis. Aqueous synthetic methods consistently produced poorly crystalline δ-MnO_2. With poorly crystalline material it is difficult to prove where in the material doped Bi is located: in the MnO_6 slabs, in the interlayer, physically connected to the MnO_2, or in separate particles entirely. To obtain more crystalline material, solid state methods were used.

Table 1. The series of Bi-doped MnO_2 materials with formula K_xBi_y-MnO_2 • nH_2O.

Name	Initial Bi:Mn Ratio	Chemical formula K_xBi_y-MnO_2	y	n	Molar Mass*
Ultra Hi-Bi	0.1	$K_{0.377}Bi_{0.156}$-MnO_2	0.156	0.32	134.18 g/mol
-	0.05	$K_{0.404}Bi_{0.084}$-MnO_2	0.084	0.31	120.31 g/mol
Hi-Bi	0.025	$K_{0.384}Bi_{0.043}$-MnO_2	0.043	0.30	110.87 g/mol
-	0.01	$K_{0.365}Bi_{0.018}$-MnO_2	0.018	0.31	104.97 g/mol
Lo-Bi	0.007	$K_{0.332}Bi_{0.013}$-MnO_2	0.013	0.27	102.63 g/mol
-	0.005	$K_{0.315}Bi_{0.010}$-MnO_2	0.010	0.30	101.29 g/mol
-	0.003	$K_{0.315}Bi_{0.006}$-MnO_2	0.006	0.31	100.58 g/mol
No-Bi	0.0	$K_{0.308}$-MnO_2	0	0.17	98.97 g/mol

*excluding H_2O

A series of Bi-doped MnO_2 materials was prepared, as detailed in **Table 1**. Resulting molar fractions of Bi in the equation K_xBi_y-MnO_2 ranged from y = 0.0 to y = 0.156. Several of these are named to discuss them easily in the manuscript. These are: the undoped material No-Bi (y = 0), Lo-Bi (y = 0.013), Hi-Bi (y = 0.043), and Ultra Hi-Bi (y = 0.156). **Fig S1** shows that the concentration of Bi^{3+} dopant could be well controlled using this method. The molar fractions of interlayer H_2O, n, were determined using thermogravimetric analysis (TGA), shown in **Fig S2**.

Bi-doping had an impact on particle size and morphology. As Bi amount increased, particle size increased, shown in **Fig 1c** with measurement details given in **Fig S3**. SEM comparison of the undoped No-Bi material (**Fig 1d**) and Ultra Hi-Bi (**Fig 1e**) showed that Bi doping increased the particle size. The layered δ-MnO_2 structure was clearly maintained in all cases, apparent by the striations running parallel to the flat surface of the particles. However, the hexagonal particle shape was no longer observed in Ultra Hi-Bi. Intermediate Bi concentrations shown in **Fig 1f-h** indicated that these changes in the material varied gradually with Bi amount.

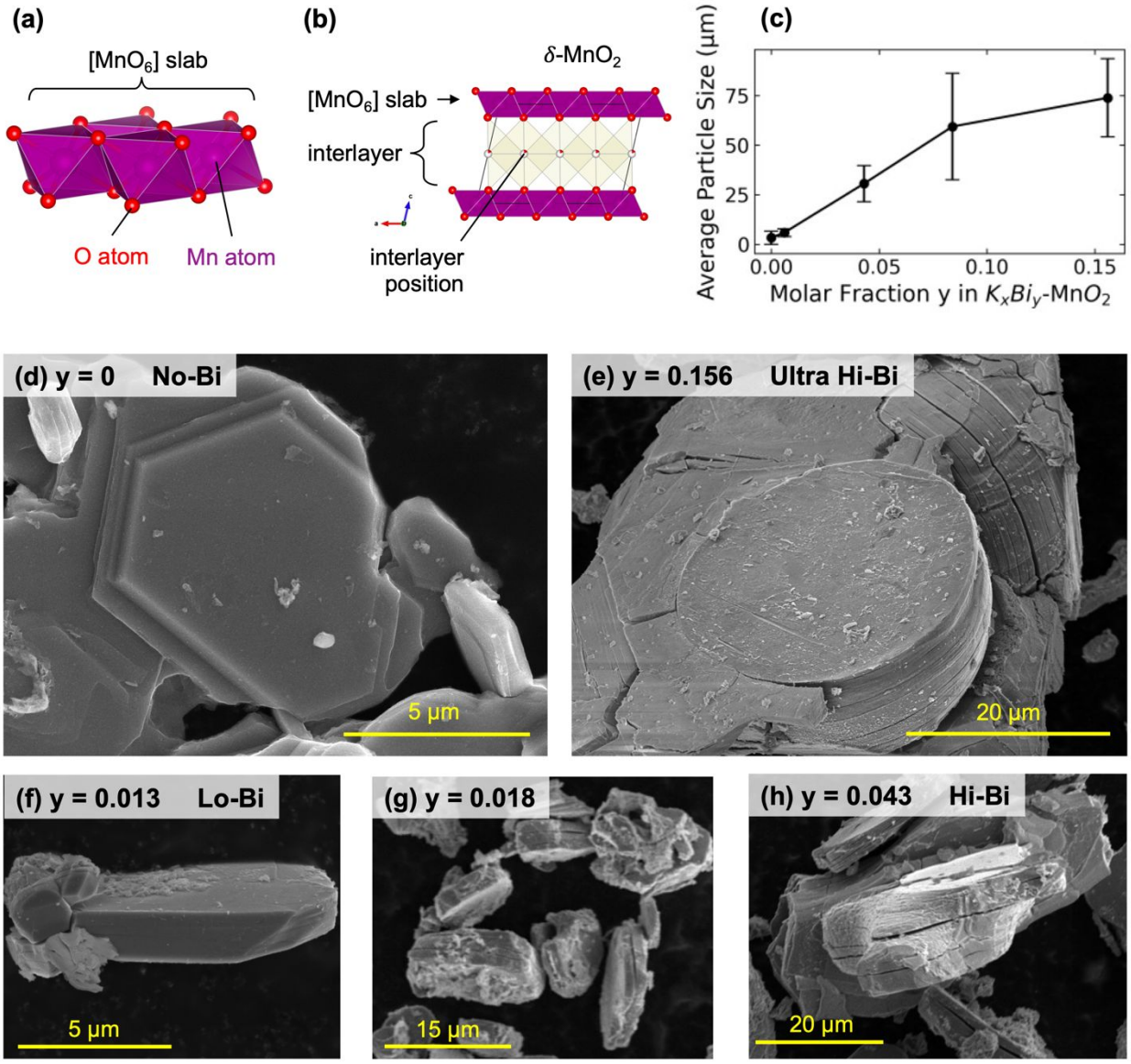

Figure 1. Morphology of the K_xBi_y-MnO_2 materials. (a) [MnO_6] slabs. (b) The structure of δ-MnO_2. (c) Particle size analysis showing that higher levels of Bi doping increased size. (d-e) SEM details of the undoped material (No-Bi, y = 0) and the highest-doped material (Ultra Hi-Bi, y = 0.156). (f-h) SEM details of materials with intermediate Bi doping: (Lo-Bi, y = 0.013), (y= 0.018), and (Hi-Bi, y = 0.043).

It has been shown that the presence of interlayer cations such as K^+ can stabilize the octahedral slabs of layered MnO_2 therefore increasing interlayer periodicity.[34] The high valence of Bi^{3+} and corresponding increased concentration of K^+ helped to stabilizes the layered structure.[35, 36] The increased thermodynamic stability of the layered configuration likely made it possible for particle size to increase as a function of y. Dopants such as Co, Ni, and Fe have been reported to substitute Mn in the octahedral MnO_2 slab, and therefore do not pillar. SEM images have showed little evidence of increased particle size with these dopants.[35, 37]

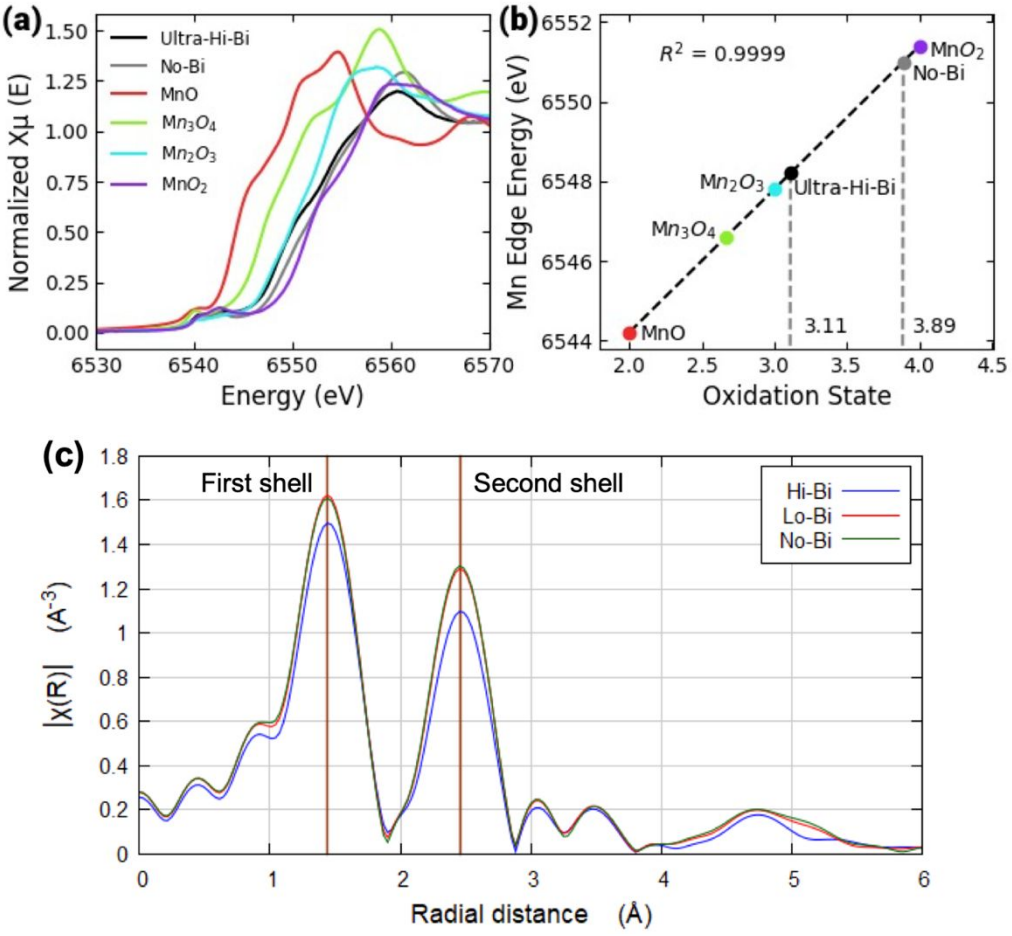

Figure 2. (a) The Mn K-edge of Ultra-Hi-Bi, No-Bi, and other Mn standards. (b) Mn redox state determined by linear regression with the Mn standards. (c) EXAFS of No-Bi, Lo-Bi, and Hi-Bi plotted in R-space.

To determine the average redox state of Mn in the materials, XAS fluorescence measurements were conducted on No-Bi and Ultra-Hi-Bi. The X-ray absorption near edge spectroscopy (XANES) of these samples was compared to a series of Mn oxide reference materials, as shown in **Fig 2a**. Linear combination fitting in **Fig 2b** indicated average Mn redox states of 3.89 and 3.11 respectively. The ICP-AES determined chemical formulas implied Mn states of 3.69 and 3.16, assuming no Mn vacancies in the material. The Ultra Hi-Bi values differed by 0.05. The values for No-Bi differed by 0.2, a larger amount. This gave evidence of Mn vacancies in the material.

Mn vacancies were explored using the extended X-ray absorption fine structure (EXAFS) region. The R-space plot in **Fig 2c** demonstrates strong peaks for the first two shells, as is standard for a layered oxide. The first shell peak, representing Mn-O scattering contributions, was consistent at 1.47 Å for all three concentrations of Bi dopant. The second shell peak, representing Mn-Mn scattering contributions, was also consistent at 2.44 Å. A structural characterization by Liu *et. al.* reported that a linear correlation between the relative heights of the first and second shells and the concentration of vacancies in the transition metal slab can be made.[38] The results yielded from applying this technique indicate ~19% vacancies in both No-Bi and Lo-Bi but a lower 16% vacancies in Hi-Bi. This would explain why the discrepancy between oxidation states from ICP and XANES was larger for the No-Bi material. These values are close to the case of 1/6 Mn vacancies described by Kuma et al (1/6 = 16.67%).[19] This is illustrated in **Fig S4**.

X-ray photoelectron spectroscopy (XPS) was also used to quantify the oxidation state of Mn and relative atomic amount of Bi to Mn, shown in **Fig S5**. As with the XANES results above, it was found that as Bi amount increased, Mn oxidation state was lowered. K/Mn atomic ratios measured by XPS were in agreement with those by ICP-AES. However, the Bi/Mn atom ratio by XPS was 7-10x higher than by ICP-AES. This suggested the possibility of a Bi-rich surface region. The extreme surface sensitivity of XPS (~10 nm) can result in quantifications that differ significantly from the bulk.

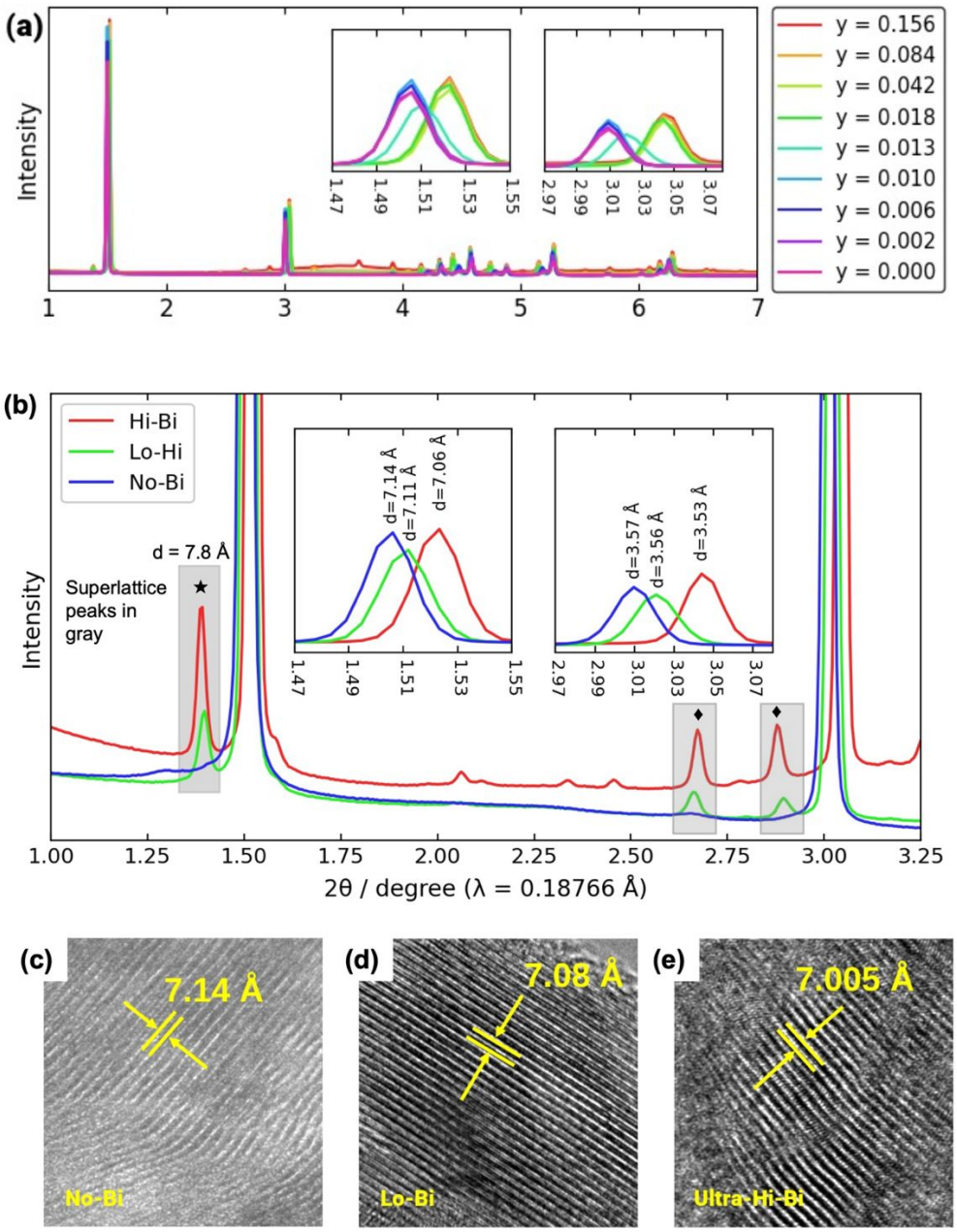

Figure 3. (a) XPD measurements were taken of K_xBi_y-MnO_2 at 9 concentrations of Bi dopant represented as molar fraction y. Insets show the reflections at ~7 Å and ~3.5 Å. (b) XPD data zoomed to show the superlattice peaks associated with interlayer cations of higher valence, highlighted in gray. (c-e) TEM images of (c) No-Bi, (d) Lo-Bi, and (e) Ultra Hi-Bi.

X-ray powder diffraction (XPD) measurements were conducted on several samples of K_xBi_y-MnO_2 at several values of y. **Fig 3a** shows the XPD at 9 values of y, using a color gradient to demonstrate changes in the reflections at 2θ = 1.51° and 3.02° (shown in the insets) as well as differences in the evolutions of peaks at higher 2θ. The large reflection at 1.51° revealed the interlayer distance, while that at 3.02° was half this distance, as expected for a layered material. The effect of Bi amount on the interlayer distance was abrupt. From y = 0-0.010 the interlayer was 7.14 Å; at y = 0.013 the value was 7.11 Å; and from y = 0.018-0.156 the value was 7.06 Å. Thus the value at 0.013 appeared to show a transition from the relatively constant upper and lower values, as emphasized in **Fig S6**. It is for this reason that the concentrations y = 0.0, y = 0.013, y = 0.043 were selected for No-Bi, Lo-Bi, and Hi-Bi. It was expected that as highly positive Bi^{3+} cations were inserted into the interlayer, the d-spacing would decrease as the negative O atoms on the slabs were screened from each other. This shift indicated that Bi^{3+} was successfully inserted into the interlayer space of layered MnO_2. Rietveld analysis of the materials is shown in **Fig S7**. Lattice parameters were refined as compared to the orthorhombic structure reported by Gaillot, et al.[39]

Fig 3b shows the patterns of No-Bi, Lo-Bi, and Hi-Bi confined to a 2θ range 1.0°-3.25°. The evolution of the peak at 2θ = 1.4° (marked by a star) made the presence of superstructures immediately apparent. Superstructures are widely reported in phyllomanganates. A prominent A = 3/2a reflection is sometimes observed, which either relates to slab vacancies or Mn^{3+}-rich rows. This peak was observed at 7.8 Å in **Fig 3b** for Lo-Bi and Hi-Bi.[17, 19, 40] Depending on the nature and amount of interlayer cations, other "characteristic" superreflections are observed in other reports. Kuma and co-workers report that heavier monovalent cations (Na^+, K^+, Cs^+) are relatively disordered in the interlayer, but partial occupancy by heavier divalent cations (Sr^{2+}, Ba^{2+}) resulted in interlayer ordering and the appearance of superlattice reflections.[19] However, superlattice reflections have also been observed by Kim et al. in K-birnessite at 2.26, 2.06, 1.73, and 1.47 Å.[32] These matched exactly with No-Bi superlattice reflections in **Fig S8**. These superlattice peaks moved and intensified with increasing Bi amount. This indicated that Bi^{3+} was in the interlayer and caused long range structural ordering of the interlayer species, including the K^+. Thus our data demonstrate that doping by small amounts of Bi^{3+} increased the crystallinity of the material. Drits and co-workers reported superlattice reflections for Ca^{2+} inserted MnO_2, which did not match the other

reflections we observed (marked by diamonds).[40] This suggests the identity of the multivalent ion in the interlayer is important to which reflections are observed.

TEM images were taken of No-Bi, Lo-Bi, and Ultra Hi-Bi, in **Fig 3c-e**. The characteristic striations of an MnO_2 layered structure make it possible to measure the interlayer d-spacing. As would be expected, an increased concentration of interlayer cations associated with increased Bi^{3+} concentration caused an interlayer contraction.[41, 42] These results were consistent with the d-spacings calculated from XPD patterns shown in **Fig 3a-b**. High angle annular dark field (HAADF) measurements were taken of Ultra Hi-Bi with energy-dispersive spectroscopy (EDS) measurements. EDS mapping shown in **Fig S9** indicated that all elemental species (O, Bi, K, and Mn) were relatively uniformly dispersed.

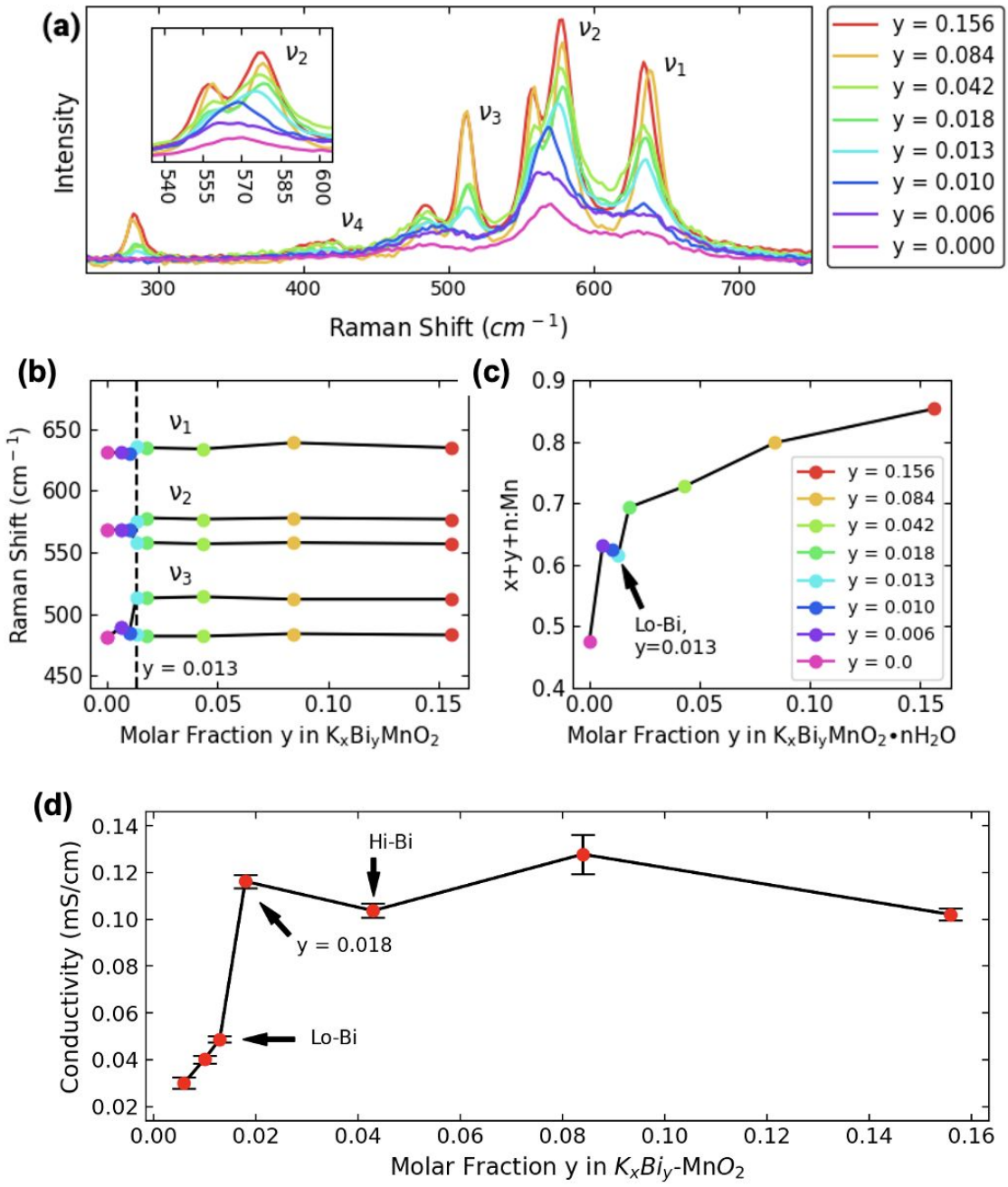

Figure 4. (a) Evolution of the Raman spectra of K_xBi_y-MnO_2 as a function of y. (b) Band shifting and splitting around y = 0.013. (c) The number of interlayer species as a function of y. (d) Conductivity values calculated from resistance measured by 4-point probe.

Raman spectra were collected of K_xBi_y-MnO_2 at various values of y, as shown in **Fig 4a.** The spectra show a direct correlation between Bi^{3+} content and Raman response. The primary observation was a sharpening of broad vibrational features into distinct peaks as the Bi^{3+} concentration exceeded y=0.013. Chen *et al.* have labeled the most predominant bands in the Raman spectra of K^+ inserted layered MnO_2 as v_1, v_2, v_3, and v_4.[43] We assume this naming convention and label the bands in **Fig 4a**. Literature assignments of birnessite-type MnO_2 assign v_1 as an in-plane Mn-O stretching while v_2 is assigned as the out-of-plane Mn-O stretching.[43-45] It should be noted, however, that Raman spectra of R-MnO_3 perovskites exhibit very similar spectra to birnessite-type MnO_2 and yet are assigned such that v_1 is an Mn-O symmetric stretch while v_2 is an R-O bending mode. v_3 is assigned as an antisymmetric stretch of the octahedra and v_4 is assigned as an octahedral tilt vibration.[46] Birnessite-type MnO_2 (monoclinic C2/m space group) is expected to have 9 Raman active modes while manganese perovskites (orthorhombic Pbnm space group) are expected to have 24. However, all spectra reported in the literature exhibit broad, convoluted spectra, preventing unambiguous identification of each mode. Here, we observe sharpening of the Raman features with increasing Bi^{3+} content, which reveals the complexity of assigning broad Raman features that are composed of many underlying peaks. We present the multiple possible assignments made previously but will refrain from making direct assignments until assignment ambiguity can be removed by future computational work.

To evaluate the quantitative changes in the spectra with varying y, the Raman spectra were fit to a sum of Lorentzian curves. Results of the deconvolution are shown in **Fig S10**, with numerical values for each y given in **Tables S4** and **S5**. Visually, there are four predominant changes in the spectra with y. The first change is the increased intensity across all peaks as y is increased. The second is the increasing intensity ratio of v_2/ v_1. The third is the narrowing of v_2 and v_3 at y=0.013 to reveal two peaks. The fourth is the appearance of a new feature at ~280 cm^{-1}. Each of these observations will be evaluated in turn.

Fits to the spectra show that as y increased, the intensity of all bands increased. This uniform increase is interpreted as an increased polarizability caused by increasing amounts of interlayer Bi^{3+}, and, potentially,

the associated higher concentrations of K^+.[47] As the amount of Bi^{3+} increases within the interlayer, increased Coulomb screening of oxygen atoms allows adjacent MnO_6 slabs to move closer together, decreasing the interlayer spacing, d, as observed by TEM and XPD.[45] This results in compression of the octahedra and a decreased cell volume, which increases the polarizability and, hence, the Raman scattering intensity across all octahedral vibrational modes. Furthermore, the intensity ratio, v_2/ v_1, shown in **Fig S11**, increases with increasing y. This has been empirically associated with cation intercalation into the interlayer, interlayer contraction, and increased interaction between layers.[43, 44, 48, 49]

Fig 4b shows the apparent splitting of both the v_2 and v_3 bands at the critical concentration y = 0.013. Since the line widths of these features are significantly reduced upon splitting, it is likely that, at y<0.013, these two bands were both present but significantly broadened, causing them to appear as one peak. While splitting of the v_3 band has been reported in the literature for layered MnO_2, splitting of the v_2 band has not.[43] The splitting of both the v_2 and v_3 bands is related to the amount of interlayer species. **Fig 4c** shows that, if ignoring the trend breaking around y = 0.013, there was a logarithmic increase in the interlayer species (K^+, Bi^{3+}, and H_2O) as Bi doping increased. The observation that both v_2 and v_3 bands narrow to reveal two features as the Bi^{3+} fraction is increased suggests increased structural ordering as the interlayers come together. The increased structural order removes inhomogeneities and improves the crystallinity, which lessens the band broadening and increases the scattering intensity.[45]

Between y = 0.042 and 0.84 the 280 cm^{-1} band became a much higher areal fraction (see **Table S4**). This may reflect a transition to a new cation arrangement in the interlayer of K^+ and Bi^{3+} to accommodate a much higher degree of occupied interlayer sites.[50] The band at 280 cm^{-1} is uncommon and to our knowledge, has only been reported in Li^+ inserted layered MnO_2 when Li is octahedrally coordinated.[45] Similar bands present themselves in Li_xCoO_2 and Li_xNiO_2 Raman spectra at 269 cm^{-1} and 256 cm^{-1}, respectively.[51] The shift of this band from 280 cm^{-1} to 269 cm^{-1} to 256 cm^{-1} is likely due to the periodic increase in atomic mass when going from Mn to Co to Ni.[47] Upon extraction of Li from Li_xCoO_2 and Li_xNiO_2 the intensity of this band decreases due to decreased density of the associated Raman active oscillators. Therefore, the appearance of this band in Bi^{3+} inserted layered MnO_2 was surprising and gave evidence of an interlayer position of

Bi^{3+}. Areal Raman mapping of the material indicated good material homogeneity, shown in **Fig S12**. The Raman response of the Bi-doped material was dependent on particle orientation (**Fig S13**), and this explained the minor variations in Raman mapping.

At the critical concentration of y = 0.013 there was a distinct change in the material, apparent from XPD, Raman, and TGA. 4-point probe resistance measurements validate that at a certain range of Bi^{3+} doping conductivity increases linearly with doping concentration before plateauing as can be seen in **Figure 4d**. With respect to conductivity, Lo-Bi was a midpoint before a sudden fundamental change in the nature of the material as Bi^{3+} content increased.

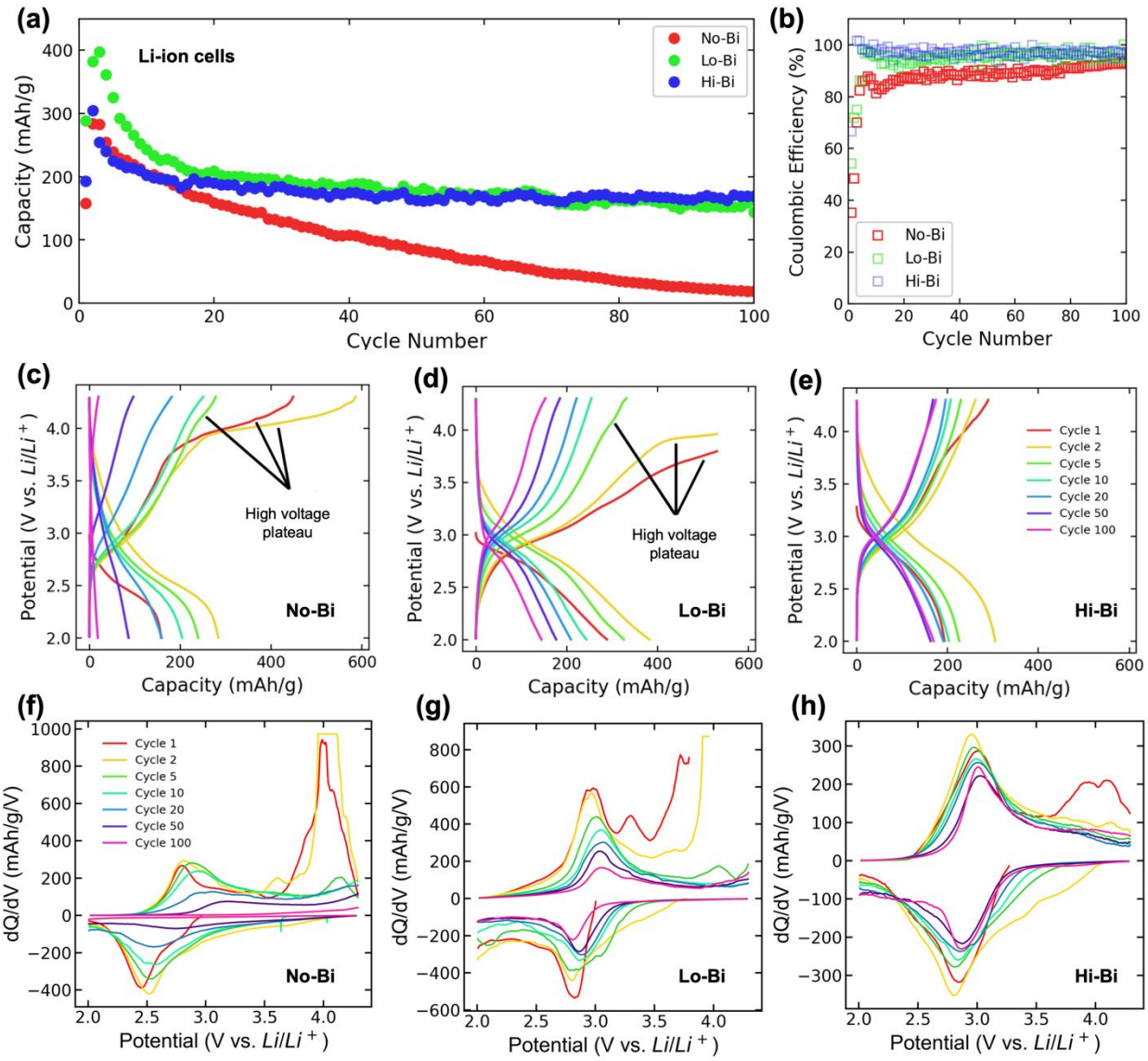

Figure 5. Li-ion batteries. (a) Capacities of No-Bi, Lo-Bi, and Hi-Bi Li-ion coin cells discharged at a rate of 22 mA/g. (b) Coulombic efficiency. (c-e) Voltage profiles of selected cycles for the No-Bi, Lo-Bi, and Hi-Bi cathodes. (f-h) Differential capacity plots for the voltage profiles above.

Li-ion cells

No-Bi, Lo-Bi, and Hi-Bi were used to fabricate cathodes at 1.5-2.5 mg/cm^2 loading of the active material. These were cycled galvanostatically at 25 mA/g (C/8 based on 200 mAh/g) against a Li foil anode, as shown in **Fig 5**. Doping the MnO_2 material with Bi enabled more stable cycling of Li^+ as compared to the undoped

MnO_2, which suffered from continual capacity decay. As shown in **Fig 5a**, Hi-Bi settled into a specific capacity of about 190 mAh/g at cycle 20 after a brief spike to higher capacity. At cycle 100 Hi-Bi was still cycling at 175 mAh/g capacity. Lo-Bi spiked to higher initial capacity but had a more significant capacity decay, about 2.5x that of Hi-Bi. Both of the Bi-doped materials were far more stable than No-Bi, which had < 20 mAh/g at cycle 100. During initial discharge, there was an electrode formation stage as the material was altered by the introduction of Li^+. During this stage there was reduced coulombic efficiency (**Fig 5b**). In the voltage profiles of **Figure 5c-e**, the initial discharges of No-Bi and Lo-Bi had lower voltage than later cycles. However the initial discharge of Hi-Bi was more consistent with later cycles. During charge, No-Bi and Lo-Bi showed high-voltage plateaus that led to low coulombic efficiency. Hi-Bi showed only a small high-voltage plateau, and only during the first charge step. Rate performance of a Lo-Bi cell is shown in **Fig S14**, where increasing rate to C/1.6 caused a 31% reduction in specific capacity. A XANES study of the charge compensation (**Fig S15**) showed that the average Mn oxidation state reduced during discharge and oxidized during charge.

The differential capacity plots in **Figure 5f-h** show the relative stability of Hi-Bi, which saw little change in the anodic/cathodic peak separation over 100 cycles. After the formation period, both Hi-Bi and Lo-Bi had a single electrochemical reaction centered at 2.9 V vs. Li. No-Bi was near 2.6 V. The irreversible electrochemical reaction associated with the high voltage plateaus was clearly evident at 4 V.

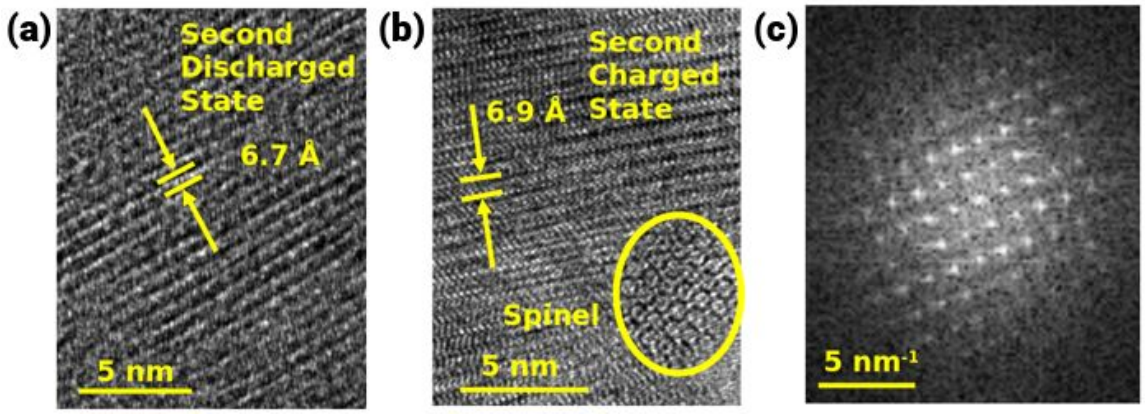

Figure 6. TEM *ex situ* images of the layered structure of Lo-Bi in Li-ion systems. (a) The second discharge state. (b) The second charge state. (c) SAED of spinel intergrowth.

Similar high voltage plateaus to those in **Fig 5** are associated with electrochemical conversion to Mn spinel.[52] Lo-Bi Li-ion cells were cycled to the end of the second discharge and second charge and disassembled for *ex situ* TEM analysis of the cathodes. In the discharged state, the MnO_2 interlayer distance was measured as 6.7 Å, shown in **Fig 6a**. In the charged state the distance was bigger, 6.9 Å, as the removal of Li^+ caused the MnO_2 slabs to repel one another, as shown in **Fig 6b**. The charged state also showed the presence of $LiMn_2O_4$ spinel (circled in yellow). **Fig 6c** shows SAED of this phase and indicated a layered spacing of 4.8 Å for the (111) layer of spinel.[52] However, during ex situ analysis, there was always the possibility that impurities observed are introduced by the dissection procedure itself.

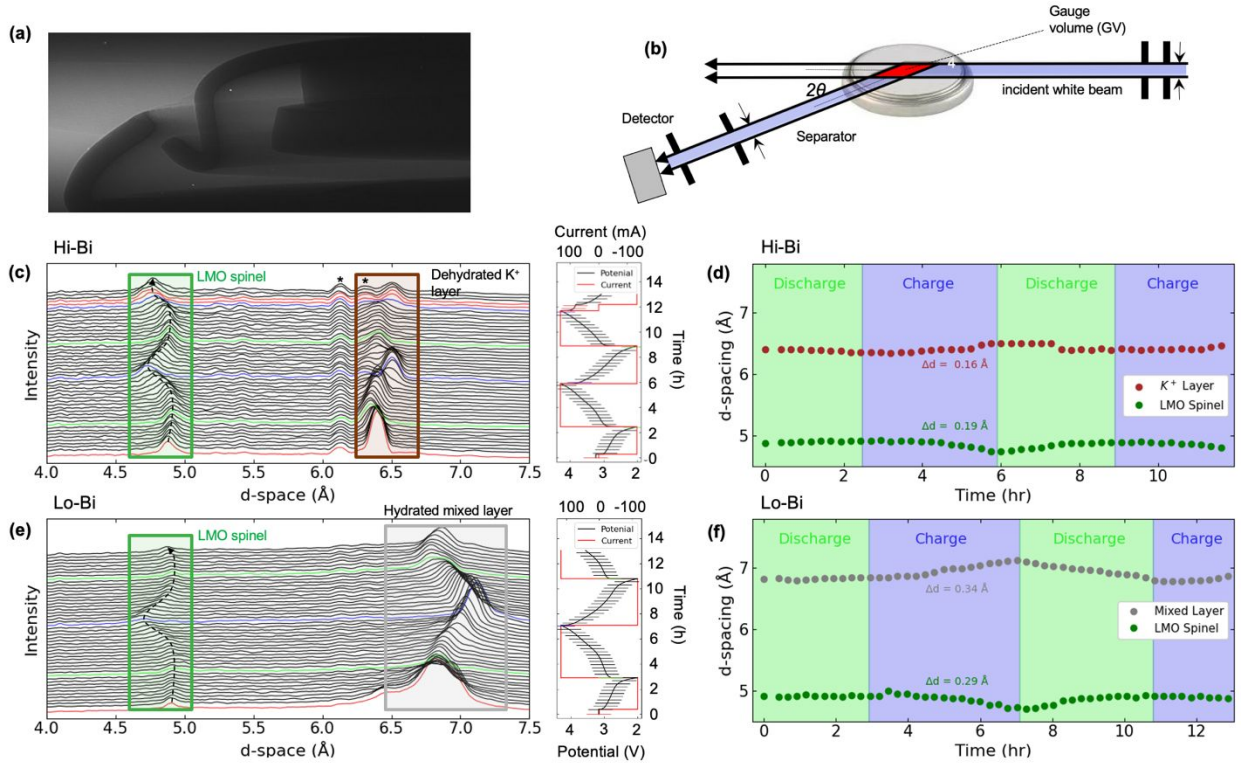

Figure 7. Operando analysis of Li-ion batteries. (a) Radiography image of a coin cell. (b) The concept of EDXRD within a hermetically sealed cell. (c) EDXRD on a Hi-Bi cathode in a Li-ion coin cell for two cycles. (d) Peak maxima for 6.4 and 4.9 Å peaks in the Hi-Bi cell. (e) EDXRD on a Lo-Bi cathode. (f) Peak maxima for 6.4 and 4.9 Å peaks in the Lo-Bi cell.

In order to study the (de)intercalation mechanism, hermetically sealed coin cells were prepared and tested using small-angle operando EDXRD. The high energy white light used for EDXRD made it possible to penetrate a steel cell casing to observe transient or non-equilibrium phases in the active material that otherwise might have "relaxed" before *in situ* or *ex situ* measurements could be taken.[53, 54] Small angle measurements were conducted at 1.5° because the two largest X-ray reflections of the K_xBi_y-MnO_2 dominated the diffraction pattern, as apparent from **Fig 3**. This angle would place the d-spacings of these reflections in the range of the photons that could penetrate the cell. It was desired to use coin cells with no Kapton windows, as we had observed that material sealed in Kapton managed to re-hydrate before analysis could be performed in laboratory settings. **Fig 7a** shows a radiography image of a coin cell penetrated by a high energy white beam, and **Fig 7b** shows the concept of EDXRD within sealed cells.

Figs 7c and **7e** show the operando EDXRD data for Li-ion cells using Hi-Bi and Lo-Bi as the cathode active materials. The initial data before cycling began was the red trace at the bottom of each plot. The starting materials in Hi-Bi and Lo-Bi were different. Additionally, cathodes made with No-Bi showed no significant crystalline pattern in the d-spacing range tested, as shown in **Fig S16**. Because this result was surprising, seven different cells fabricated in two different batches were tested, and it was found that the crystalline layered structure of No-Bi did not survive within any fabricated cells. It should be noted that the two small, invariant peaks marked by stars in the Hi-Bi system were caused by Bi fluorescence, as detailed in **Fig S17**. The Bi concentration in the Lo-Bi system was not high enough to produce these fluorescence peaks. An accounting of the uncycled materials in each cell is given in **Table S1**.

In Hi-Bi **Fig 7c** showed a peak at 6.4 Å in the uncycled material due to the dehydrated K^+-inserted layered MnO_2 phase.[55, 56] This contracted potassiated phase would likely hydrate and convert back to ~7 Å δ-MnO_2 or decompose if exposed to air for *ex situ* measurements.[57-61] The peak at 4.9 Å was due to presence of the $LiMn_2O_4$ (LMO) phase in the pristine cathode. Upon cycling, LMO displayed electrochemical inactivity below 3.0 V on charge and discharge, as expected. The 6.4 Å peak contracted during discharge (intercalation of Li^+) and expanded during charge (deintercalation of Li^+).

In contrast, Lo-Bi in **Fig 7e** initially had a hydrated, layered MnO_2 peak at 6.8 Å as well as an $LiMn_2O_4$ (LMO) spinel peak at 4.9 Å. In the pristine material there was partial peak separation possibly indicating a partial insertion of Li^+, sourced from the electrolyte, leading to distinct layered phases of either Li^+, K^+ or H_2O inserted into partially segregated layers. In this pristine state, Li^+ and K^+ may be occupying positions adjacent to H_2O as this would maintain a 6.9 Å interlayer distance. It should be noted that hydrated $LiMnO_2$, $NaMnO_2$, and $KMnO_2$ all have an interlayer d-spacing of around 7 Å.[62, 63] A pure dehydrated layered Li_xMnO_2 phase would have a d-spacing around 4.8 Å depending on the value of x.[64] However, the cycling behavior revealed the 4.9 Å peak was LMO spinel, due to the peak shifting observed: d-spacing expanded during electrochemical insertion of Li^+ and contracted on extraction.[65, 66] For Li_xMnO_2 material, the opposite trend would be expected: d-spacing contraction during electrochemical insertion of Li^+. However, it should be noted the LMO reaction (~3.5 V) was small in differential capacity plots, suggesting it was a small fraction of the overall capacity.

Bi doping in the Hi-Bi cell resulted in a different starting material in the cell than Lo-Bi. Analysis of this material during (de)intercalation of Li^+ revealed that the dehydrated K^+ inserted MnO_2 layer shifted minimally, shown in **Fig 7d**. This was due to the presence of large interlayer species such as K^+ and Bi^{3+} pillaring and stabilizing the interlayer spacing and preventing excessive interlayer expansion or contraction. This explains the increased capacity retention of Hi-Bi in **Fig 5a**. The change in d-spacing of the hydrated 6.9 Å peak in Lo-Bi was over 2x as much, shown in **Fig 7f**. This led to increased degradation of the active material.

Removal of K^+ from the interlayer of K_xBi_y-MnO_2 would leave the pillaring Bi^{3+} and allow more interlayer sites for Li^+ intercalation, so this was attempted (**Fig S18**). However, it was found that this resulted in reduced performance (**Fig S19**), as the large K^+ played a role in pillaring with the Bi^{3+}.[34-36]

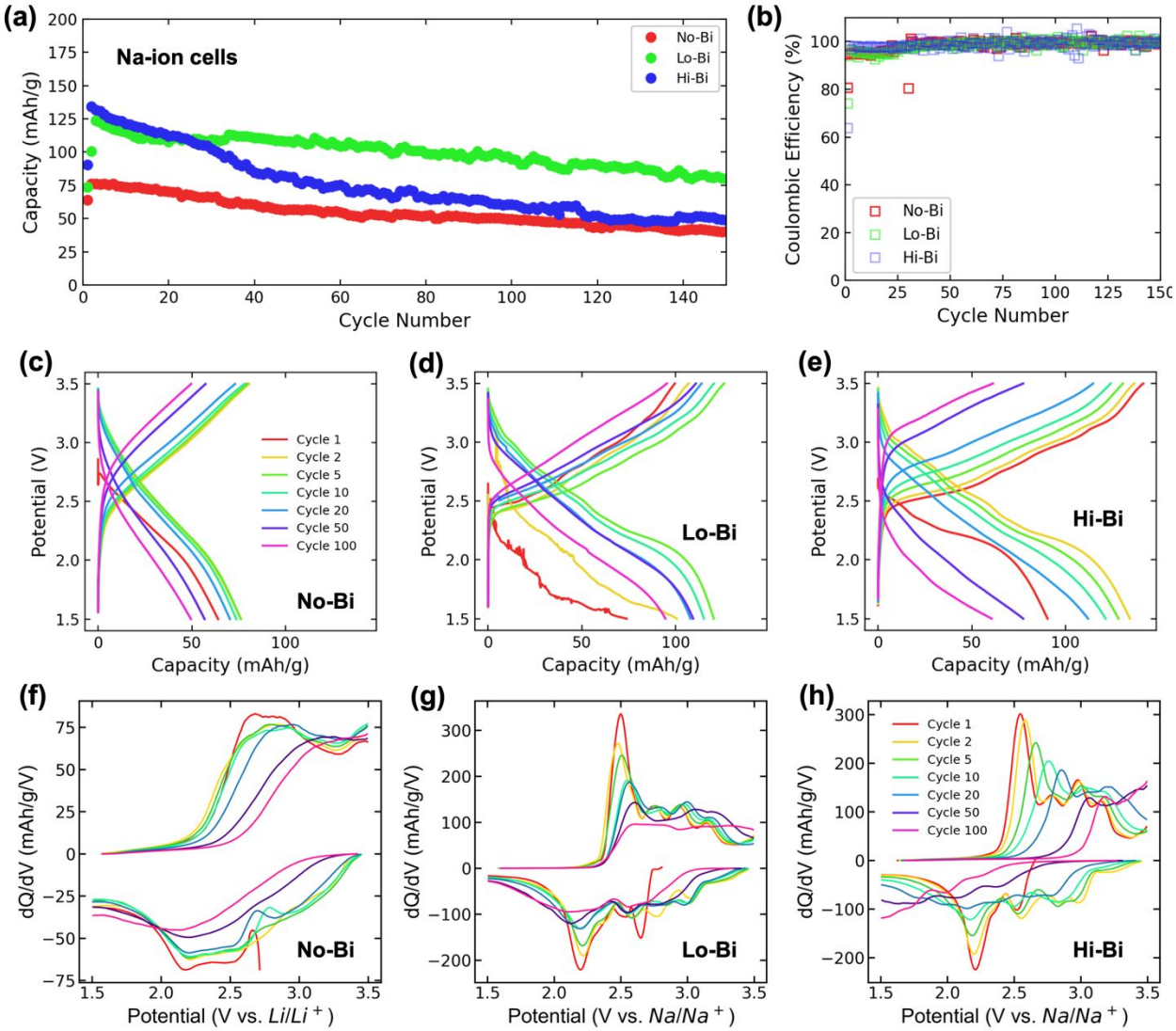

Figure 8. Na-ion batteries. (a) Capacities of No-Bi, Lo-Bi, and Hi-Bi Li-ion coin cells discharged at a rate of 45 mA/g. (b) Coulombic efficiency. (c-e) Voltage profiles of selected cycles for the No-Bi, Lo-Bi, and Hi-Bi cathodes. (f-h) Differential capacity plots for the voltage profiles above.

Na-ion cells

Analogous Na-ion batteries were fabricated for comparison to the Li-ion batteries presented in the previous section. This would allow us to assess the effect of the working cation size. Li^+ is 90 pm, but Na^+ is 116 pm and close to the size of Bi^{3+} at 117 pm. K^+ at 152 pm was by far the largest interlayer cation in this work.

No-Bi, Lo-Bi, and Hi-Bi were used to fabricate cathodes at 1.3 mg/cm^2 loading of the active material. These were cycled galvanostatically at 45 mA/g against a Na foil anode (C/4.4 based on 200 mAh/g), shown in **Figure 8**. Na^+ (de)intercalation in No-Bi was not as unstable as that of Li^+. However, specific capacity was significantly increased by Bi doping. After an initial formation cycle, both Hi-Bi and Lo-Bi were about 125 mAh/g, while No-Bi was 75 mAh/g, as shown in **Figure 8a**. In the Na-ion system the presence of high voltage plateaus was not observed in any of the voltage curves for No-Bi, Hi-Bi, or Lo-Bi, as Na^+ is too large to favorable allow for the formation of spinel.[67] From the differential capacity plots in **Figure 8e-g** the No-Bi case had large peak separation that increased at greater cycle numbers. Lo-Bi and Hi-Bi had four distinct electrochemical peaks on both charge and discharge, which can be seen as plateaus in the voltage profiles (**Figures 8c** and **8d**). These may be associated with the gliding of MnO_2 octahedral slabs.[62, 68] It is known that Na_xMO_2 systems display many ordered phases.[69-71] While the best Li-ion cathode was Hi-Bi, this was not true for the Na-ion system. **Figure 8a** shows that Hi-Bi cathodes decayed more quickly than the other cells. Voltage decay was also more severe in the Hi-Bi case, and the Lo-Bi peaks were more stable in **Fig 8g** than those in **Fig 8h**.

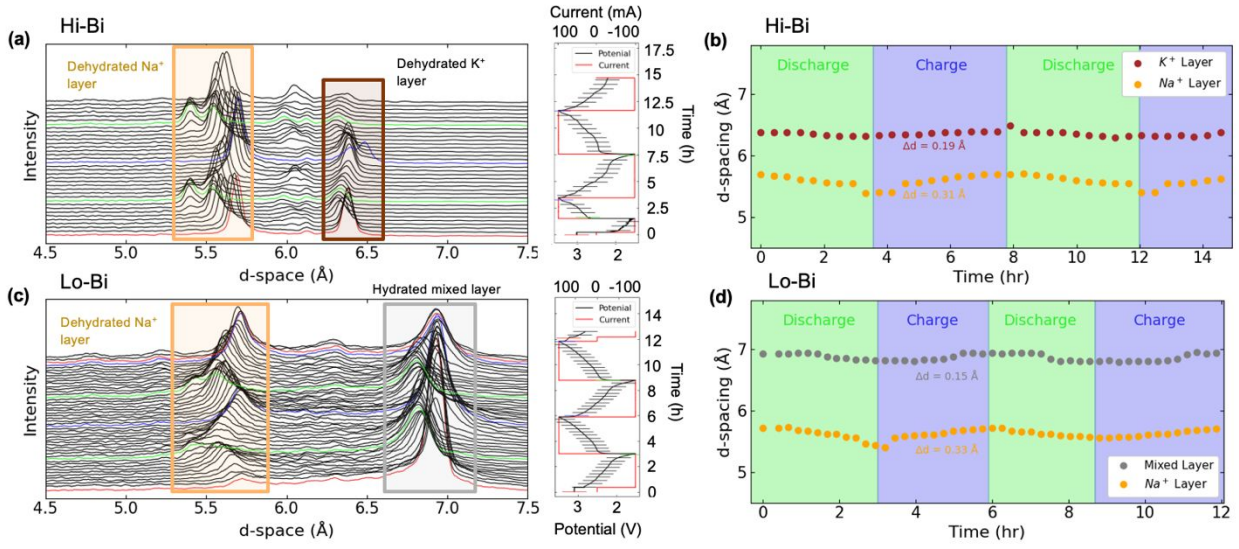

Figure 9. Operando analysis of Na-ion batteries. (a) EDXRD on a Hi-Bi cathode in a Na-ion coin cell. (b) Peak maxima for 5.6 and 4.9 Å peaks in the Hi-Bi cell. (c) EDXRD on a Lo-Bi cathode. (d) Peak maxima during cycling for 5.6 and 4.9 Å peaks in the Lo-Bi cell.

Figures 9a and **9c** show the operando EDXRD data for Na-ion cells using Hi-Bi and Lo-Bi as the cathode active materials. The initial data before cycling began was the red trace at the bottom of each plot. As in the case of the Li-ion cells, the initial materials in Hi-Bi and Lo-Bi were different from each other, and also differed from the as-synthesized materials. Hi-Bi (**Figure 9a**) showed a peak at 6.4 Å in the pristine material, indicating the dehydrated K^+ inserted layered MnO_2 phase.[56] As was the case with the Li-ion cells, the hydrated ~6.9 Å birnessite peak was not present with the Hi-Bi material. The peak at 5.7 Å was consistent with prior literature reports of dehydrated Na^+ inserted layered MnO_2.[72-74] Reports of 5.7 Å Na^+ inserted layered MnO_2 are common throughout the literature, but reports of 5.7 Å K^+ inserted layered MnO_2 in molar fractions of K:Mn greater than 0.22 are sparse if not non-existent.[75-79] Layered MnO_2 inserted with K^+ cannot contract significantly below 6.4 Å due to the large ionic radius of K^+. An accounting of the uncycled materials in each cell is given in **Table S1**.

The Lo-Bi cell in **Figure 9c** initially had the dehydrated 5.7 Å Na^+ inserted layered MnO_2 peak, although to a much smaller extent than the Hi-Bi cell. The 6.9 Å hydrated, mixed MnO_2 layer typical of birnessite was the majority material. Thus the Lo-Bi Na-ion cell was similar to the Li-ion cell in that the hydrated layer was present at a d-spacing slightly lower than that of the as-synthesized material. A clear finding was that Bi doping at the level of Hi-Bi promoted dehydration of the layered MnO_2 structure, regardless of the cations in the electrolyte. Doping at the Lo-Bi level retained the hydrated layer in both systems.

In Lo-Bi the overall intensity of the 5.7 Å peak increased as cycling continued (**Figure 9c**). The shifting of the 5.7 Å peak indicated the expected behavior of an interlayer contraction during Na^+ insertion and expansion during Na^+ extraction. The sudden shift of the 5.7 Å peak at the end of discharge may be explained by cation rearrangement in the interlayer to a lower energy configuration allowing for further contraction of the interlayer, and/or conversion from octahedral to prismatic coordination of Na^+ further evidenced by the accompanying voltage drop and the time lag for deformation of the new peak.[50, 62]

The 6.9 Å peak shifted in only a portion of discharge and charge process (**Figure 9d**). It shifted as expected on discharge from 3.5 V to 2.2 V. However, on further discharge from 2.2 V to 1.5 V and on charging back to 2.6 V it showed almost no change in intensity or position. This may indicate that Na^+ was preferentially inserting into the 5.7 Å phase in this regime. Conversely, it may indicate a stabilization of the interlayer spacing in this regime, reducing volume expansion of the unit cell, potentially leading to increased reversibility.[68, 80, 81] This second possibility was evinced by a lack of an increase in intensity of the 5.7 Å during this period. Stabilization of the hydrated mixed layer offered by low amounts of Bi^{3+} doping may be beneficial to Na-ion batteries due to increased interlayer distance. This would accommodate the larger radius of Na^+ as compared to Li^+. Li and co-workers have reported that the presence of crystal water is beneficial for Na-ion cycling.[82] In the present work, the lower concentration of Bi^{3+} offered optimal pillaring to allow for better capacity retention in Lo-Bi. This led to capacity retention of over 100 mAh/g after 100 cycles for Lo-Bi compared to the below 75 mAh/g in either No-Bi or Hi-Bi.

The data showed that Lo-Bi was the better cathode for Na-ion cycling, while Hi-Bi was the better cathode for Li-ion cycling. Here the performance was judged by stability of the specific capacity during cycling, as well as by voltage retention, i.e. maintaining a high voltage during discharge. Our hypothesis for this result is that a larger interlayer distance was better matched to the larger Na^+ working ion, and a smaller interlayer was better matched to the smaller Li^+. Since Lo-Bi maintained a larger ~6.9 Å hydrated interlayer, this was the reason it showed better stability in Na-ion cells. And since Hi-Bi showed a loss of crystal water, the resulting smaller, dehydrated ~6.4 Å interlayer was more stable during Li-ion cycling.

Conclusions

This work has provided insight into the structure and morphology of Bi-doped layered MnO_2, which also had K^+ cations in the interlayer. This material was stable for longer times in ambient conditions than Bi-doped MnO_2 with interlayer Na^+. While Bi-doped δ-MnO_2 has been reported previously for Li-ion cathodes, our study presents structural characterization, including operando experiments, to provide evidence that Bi is pillaring the material. To our knowledge ours is the first to report this work for Na-ion cathodes.

Our purpose in executing this work was to provide evidence of cation pillaring, in particular Bi pillaring of layered δ-MnO_2. Bi^{3+} pillaring of MnO_2 has been mentioned in the literature for decades, but experimental evidence of the effect is difficult to pinpoint. As a definition of pillaring, we assume it to mean that a pillar improves stability of a layered material by reducing deformation during electrochemical activity. In effect, this means the pillar "pins" the layers in place.[28] This work provides substantial evidence that δ-K_xBi_y-MnO_2 was synthesized with Bi^{3+} located in the interlayer. XRD and TEM in **Fig 3** demonstrated that Bi amount had an impact on interlayer distance, but this could also have been caused by an associated increase in K^+ amount. However, Raman spectra in **Fig 4** showed that increasing Bi amount caused a split in the δ-MnO_2 v_2 band. K^+ is known to split the v_3 band, but not the v_2 band. Introduction of Bi^{3+} also caused the appearance of a band at 280 cm^{-1}, which was strong evidence of an interlayer position of Bi^{3+}. Addition of Bi also affected superstructure reflections related to the other interlayer cations (K^+) and Mn vacancies. This meant that Bi increased ordering in the layered structure. During electrochemical cycling of both Li-ion and Na-ion cathodes, Bi increased the stability, as measured by specific capacity and voltage retention. During operando EDXRD experiments, higher stability was accompanied by a reduced change in d-spacing (Δd) during (de)intercalation of the working ion (**Figs 7d** and **9d**). This was evidence of the "pinning" effect.

Results of the Li-ion cell experiments showed that Bi doping at both the Lo-Bi and Hi-Bi levels allowed the crystal structure of the material to be maintained and allowed for more stable cell cycling than undoped K_x-MnO_2. However, cells made with the Hi-Bi material, amounting to 4.3% doping of Bi, were more stable. These cycled at 175-190 mAh/g specific capacity through the first 100 cycles with a nominal voltage of 2.9 V. In situ experiments to characterize the cathodes within sealed cells showed that Hi-Bi doping promoted dehydration of the K_xBi_y-MnO_2 interlayer, which had a distance of 6.4 Å. This matched the reported interlayer distance of dehydrated K-birnessite. In contrast, Lo-Bi had a hydrated interlayer near 6.9 Å in size. During Li^+ cycling, the 6.4 Å dehydrated interlayer of Hi-Bi expanded and contracted far less than the 6.9 Å hydrated interlayer of Lo-Bi. Both materials showed some conversion to LMO spinel, which also cycled reversibly. However, the LMO reaction was small in differential capacity plots, suggesting this was a small fraction of the overall capacity. Previous reports have suggested that Bi doping of 20% result in

stabilized Li-ion cycling in layered MnO_2.[31] However, these reports involved largely amorphous active material. Our results showed that Bi doping of only 1.3% (Lo-Bi) provided a large stability benefit.

In the Na-ion system, both Hi-Bi and Lo-Bi systems showed a 5.7 Å dehydrated Na+ inserted layer when analyzed in situ. Lo-Bi also showed the hydrated 6.9 Å layer, while the Hi-Bi material provoked dehydration of the layered structure, meaning the 6.9 Å layer was absent for Hi-Bi just like in the Li-ion cells. For Na-ion cells, the desired Bi doping level for superior capacity and stability was the Lo-Bi material. This showed that maintaining the presence of crystal water in the hydrated 6.9 Å layer was important for reversible Na-ion cycling. This led to capacity retention of over 100 mAh/g after 100 cycles for Lo-Bi compared to the below 75 mAh/g in either No-Bi or Hi-Bi. The nominal voltage was about 2.5 V. The undoped No-Bi material was not as unstable for the Na-ion system as in Li-ion cells.

Author Information

Corresponding Author

*Email: j.gallaway@northeastern.edu (J. Gallaway)

Author contributions

Matthew A. Kim: Methodology; Investigation, Formal Analysis, and Visualization (Synthesis, materials characterization, XANES, XPD, Raman, EDXRD, battery fabrication and cycling); Writing – original draft. **Eric K. Zimmerer**: Investigation, Formal Analysis, and Visualization (EXAFS, XANES); Writing – review and editing. **Zachary T. Piontkowski**: Formal analysis (Raman); Writing – review and editing. **Mark A. Rodriguez**: Formal analysis (Rietveld). **Noah B. Schorr**: Investigation (conductivity). **Bryan R. Wygant**: Investigation (XPS). **John S. Okasinski**: Investigation (EDXRD). **Andrew C. Chuang**: Investigation (EDXRD). **Timothy N. Lambert**: Methodology; Writing – review and editing. **Joshua W. Gallaway**: Conceptualization; Methodology; Supervision; Formal Analysis; Writing – original draft; Writing – review and editing.

Conflicts of interest

There are no known conflicts to declare.

Acknowledgments

This work was supported by the U.S. Department of Energy (DOE) Office of Electricity Delivery and Energy Reliability, Dr. Imre Gyuk, Energy Storage Program Manager. This research used resources of the Advanced Photon Source beamline 6-BM, a U.S. Department of Energy (DOE) Office of Science User Facility operated for the DOE Office of Science by Argonne National Laboratory under Contract No. DE-AC02-06CH11357. This research also used resources at beamlines 7-BM (QAS) and 28-ID-2 (XPD) of the National Synchrotron Light Source II, a U.S. Department of Energy (DOE) Office of Science User Facility operated for the DOE Office of Science by Brookhaven National Laboratory under Contract No. DE-SC0012704. This work was performed, in part, at the Center for Integrated Nanotechnologies, an Office of Science User Facility operated for the U.S. Department of Energy (DOE) Office of Science. We thank Bebi Patil for synthesis assistance. We thank Alyssa Stavola for assistance with EDXRD. We thank Sanjit K. Ghose for running the XPD samples at NSLS-II during the COVID-19 pandemic. The views expressed in this article do not necessarily represent the views of the U.S. Department of Energy or the United States Government. This article has been authored by an employee of National Technology & Engineering Solutions of Sandia, LLC under Contract No. DE-NA0003525 with the U.S. Department of Energy (DOE). The National Technology & Engineering Solutions of Sandia, LLC employee owns all right, title and interest to their contribution to the article and is responsible for its contents. The United States Government retains and the publisher, by accepting the article for publication, acknowledges that the United States Government retains a non-exclusive, paid-up, irrevocable, world-wide license to publish or reproduce the published form of this article or allow others to do so, for United States Government purposes. The DOE will provide public access to these results of federally sponsored research in accordance with the DOE Public Access Plan https://www.energy.gov/downloads/doe-public-access-plan.

References

1. M. M. Thackeray, *Progress in Solid State Chemistry*, 1997, **25**, 1-71.

2. D. E. Turney, G. G. Yadav, J. W. Gallaway, S. Kolhekar, J. Huang, M. J. D'Ambrose and S. Banerjee, in *Energy-Sustainable Advanced Materials*, Springer, 2021, pp. 1-26.

3. G. P. Wheeler, L. Wang and A. C. Marschilok, *Elements in Grid Energy Storage*.

4. Y. Chabre and J. Pannetier, *Progress in Solid State Chemistry*, 1995, **23**, 1-130.

5. R. Korthauer, *Lithium-ion batteries: basics and applications*, Springer, 2018.

6. I. Davidson, R. McMillan, J. Murray and J. Greedan, *Journal of power sources*, 1995, **54**, 232-235.

7. G. Vitins and K. West, *Journal of the Electrochemical Society*, 1997, **144**, 2587.

8. T. Uyama, K. Mukai and I. Yamada, *RSC advances*, 2018, **8**, 26325-26334.

9. A. R. Armstrong and P. G. Bruce, *Nature*, 1996, **381**, 499-500.

10. S. Mishra and G. Ceder, *Physical Review B*, 1999, **59**, 6120.

11. F. Schipper, E. M. Erickson, C. Erk, J.-Y. Shin, F. F. Chesneau and D. Aurbach, *Journal of The Electrochemical Society*, 2016, **164**, A6220.

12. Y. I. Jang, B. Huang, Y. M. Chiang and D. R. Sadoway, *Electrochemical and solid-state letters*, 1998, **1**, 13.

13. G. Ceder and S. Mishra, *Electrochemical and solid-state letters*, 1999, **2**, 550.

14. J. Kim and A. Manthiram, *Nature*, 1997, **390**, 265-267.

15. J. Paulsen, C. Thomas and J. Dahn, *Journal of the Electrochemical Society*, 1999, **146**, 3560.

16. N. Yabuuchi, R. Hara, M. Kajiyama, K. Kubota, T. Ishigaki, A. Hoshikawa and S. Komaba, *Advanced Energy Materials*, 2014, **4**, 1301453.

17. V. A. Drits, E. Silvester, A. I. Gorshkov and A. Manceau, *Am Mineral*, 1997, **82**, 946-961.

18. S. Boyd, N. R. Geise, M. F. Toney and V. Augustyn, *Frontiers in chemistry*, 2020, **8**, 715.

19. K. Kuma, A. Usui, W. Paplawsky, B. Gedulin and G. Arrhenius, *Mineral Mag*, 1994, **58**, 425-447.

20. F. Le Cras, S. Rohs, M. Anne and P. Strobel, *Journal of power sources*, 1995, **54**, 319-322.

21. R. Chen and M. S. Whittingham, *Journal of The Electrochemical Society*, 1997, **144**, L64.

22. B. J. Kwon, L. Yin, C. J. Bartel, K. Kumar, P. Parajuli, J. Gim, S. Kim, Y. A. Wu, R. F. Klie and S. H. Lapidus, *Chemistry of Materials*, 2022, **34**, 836-846.

23. S.-D. Han, S. Kim, D. Li, V. Petkov, H. D. Yoo, P. J. Phillips, H. Wang, J. J. Kim, K. L. More and B. Key, *Chemistry of Materials*, 2017, **29**, 4874-4884.

24. B. J. Kwon, C. Kim, J. R. Jokisaari, H. D. Yoo, S.-D. Han, S. Kim, K.-C. Lau, C. Liao, Y.-S. Liu and J. Guo, *Chemistry of Materials*, 2020, **32**, 6014-6025.

25. J. B. Mitchell, R. Wang, J. S. Ko, J. W. Long and V. Augustyn, *Journal of The Electrochemical Society*, 2022, **169**, 030534.

26. M. A. Dzieciuch, N. Gupta and H. S. Wroblowa, *Journal of the Electrochemical Society*, 1988, **135**, 2415-2418.

27. A. M. Bruck, M. A. Kim, L. Ma, S. N. Ehrlich, J. S. Okasinski and J. W. Gallaway, *Journal of the Electrochemical Society*, 2020, 110514.

28. V. Augustyn, R. Wang, N. Balke, M. Pharr and C. B. Arnold, *ACS Energy Letters*, 2020, **5**, 3548-3559.

29. T. B. Atwater and A. J. Salkind, *Journal of the Electrochemical Society*, 1998, **145**, L31.

30. S. Bach, J.-P. Pereira-Ramos, C. Cachet, M. Bode and L. T. Yu, *Electrochimica acta*, 1995, **40**, 785-789.

31. J. Yang, T. B. Atwater and J. J. Xu, *Journal of power sources*, 2005, **139**, 274-278.

32. S. H. Kim, S. J. Kim and S. M. Oh, *Chem Mater*, 1999, **11**, 557-563.

33. A. Rutt, J.-X. Shen, M. Horton, J. Kim, J. Lin and K. A. Persson, *arXiv preprint arXiv:2204.05383*, 2022.

34. T. Hatakeyama, N. L. Okamoto and T. Ichitsubo, *Journal of Solid State Chemistry*, 2022, **305**, 122683.

35. A. Ogata, S. Komaba, R. Baddour-Hadjean, J.-P. Pereira-Ramos and N. Kumagai, *Electrochimica Acta*, 2008, **53**, 3084-3093.

36. R. Kempaiah, H. Chan, S. Srinivasan, S. K. Sankaranarayanan, B. Narayanan and A. Subramanian, *ACS Applied Energy Materials*, 2021, **4**, 12099-12111.

37. H. Yin, F. Liu, X. Feng, T. Hu, L. Zheng, G. Qiu, L. K. Koopal and W. Tan, *Geochimica Et Cosmochimica Acta*, 2013, **117**, 1-15.

38. J. Liu, L. Yu, E. Hu, B. S. Guiton, X.-Q. Yang and K. Page, *Inorganic Chemistry*, 2018, **57**, 6873-6882.

39. A.-C. Gaillot, V. A. Drits, A. Manceau and B. Lanson, *Microporous and Mesoporous Materials*, 2007, **98**, 267-282.

40. V. A. Drits, B. Lanson, A. I. Gorshkov and A. Manceau, *Am Mineral*, 1998, **83**, 97-118.

41. S. Fleischmann, M. A. Spencer and V. Augustyn, *Chemistry of Materials*, 2020, **32**, 3325-3334.

42. O. Ghodbane, F. Ataherian, N.-L. Wu and F. Favier, *Journal of Power Sources*, 2012, **206**, 454-462.

43. D. Chen, D. Ding, X. Li, G. H. Waller, X. Xiong, M. A. El-Sayed and M. Liu, *Chemistry of Materials*, 2015, **27**, 6608-6619.

44. S. Boyd, K. Ganeshan, W.-Y. Tsai, T. Wu, S. Saeed, D.-e. Jiang, N. Balke, A. C. van Duin and V. Augustyn, *Nat Mater*, 2021, **20**, 1689-1694.

45. C. Julien, M. Massot, R. Baddour-Hadjean, S. Franger, S. Bach and J. Pereira-Ramos, *Solid State Ionics*, 2003, **159**, 345-356.

46. L. Martín-Carrón, A. De Andres, M. Martínez-Lope, M. Casais and J. Alonso, *Physical Review B*, 2002, **66**, 174303.

47. J. R. Ferraro, *Introductory raman spectroscopy*, Elsevier, 2003.

48. Q. Zhang, M. D. Levi, Q. Dou, Y. Lu, Y. Chai, S. Lei, H. Ji, B. Liu, X. Bu and P. Ma, *Advanced Energy Materials*, 2019, **9**, 1802707.

49. P. Scheitenberger, H. Euchner and M. Lindén, *Journal of Materials Chemistry A*, 2021, **9**, 18466-18476.

50. J. Vinckeviciute, M. D. Radin and A. Van der Ven, *Chemistry of Materials*, 2016, **28**, 8640-8650.

51. C. Julien, *Solid State Ionics*, 2000, **136**, 887-896.

52. M. Gu, I. Belharouak, J. Zheng, H. Wu, J. Xiao, A. Genc, K. Amine, S. Thevuthasan, D. R. Baer and J.-G. Zhang, *ACS nano*, 2013, **7**, 760-767.

53. J. W. Gallaway, C. K. Erdonmez, Z. Zhong, M. Croft, L. A. Sviridov, T. Z. Sholklapper, D. E. Turney, S. Banerjee and D. A. Steingart, *Journal of Materials Chemistry A*, 2014, **2**, 2757-2764.

54. A. C. Marschilok, A. M. Bruck, A. Abraham, C. A. Stackhouse, K. J. Takeuchi, E. S. Takeuchi, M. Croft and J. W. Gallaway, *Physical Chemistry Chemical Physics*, 2020, **22**, 20972-20989.

55. P. LE, 2003.

56. H. Kim, D. H. Seo, J. C. Kim, S. H. Bo, L. Liu, T. Shi and G. Ceder, *Advanced materials*, 2017, **29**, 1702480.

57. C. Vaalma, G. A. Giffin, D. Buchholz and S. Passerini, *Journal of The Electrochemical Society*, 2016, **163**, A1295.

58. M. K. Cho, J. H. Jo, J. U. Choi and S.-T. Myung, *ACS applied materials & interfaces*, 2019, **11**, 27770-27779.

59. R. Chen, P. Zavalij and M. S. Whittingham, *Chemistry of Materials*, 1996, **8**, 1275-1280.

60. E. A. Johnson and J. E. Post, *American Mineralogist*, 2006, **91**, 609-618.

61. P. F. Wang, Y. You, Y. X. Yin and Y. G. Guo, *Advanced Energy Materials*, 2018, **8**, 1701912.

62. M. H. Han, E. Gonzalo, M. Casas-Cabanas and T. Rojo, *Journal of Power Sources*, 2014, **258**, 266-271.

63. M. Nakayama, T. Kanaya, J.-W. Lee and B. N. Popov, *Journal of Power Sources*, 2008, **179**, 361-366.

64. P. Bruce, A. áRobert Armstrong and R. Gitzendanner, *Journal of Materials Chemistry*, 1999, **9**, 193-198.

65. F. Luo, C. Wei, C. Zhang, H. Gao, J. Niu, W. Ma, Z. Peng, Y. Bai and Z. Zhang, *Journal of Energy Chemistry*, 2020, **44**, 138-146.

66. C. Tomon, S. Sarawutanukul, N. Phattharasupakun, S. Duangdangchote, P. Chomkhuntod, N. Joraleechanchai, P. Bunyanidhi and M. Sawangphruk, *Communications Chemistry*, 2022, **5**, 1-12.

67. J.-Y. Hwang, S.-T. Myung and Y.-K. Sun, *Chemical Society Reviews*, 2017, **46**, 3529-3614.

68. M. D. Radin, J. Alvarado, Y. S. Meng and A. Van der Ven, *Nano letters*, 2017, **17**, 7789-7795.

69. C. Delmas, D. Carlier and M. Guignard, *Advanced Energy Materials*, 2021, **11**, 2001201.

70. Q. Liu, Z. Hu, M. Chen, C. Zou, H. Jin, S. Wang, S. L. Chou and S. X. Dou, *Small*, 2019, **15**, 1805381.

71. R. Berthelot, D. Carlier and C. Delmas, *Nature materials*, 2011, **10**, 74-80.

72. L. Yang, X. Li, X. Ma, S. Xiong, P. Liu, Y. Tang, S. Cheng, Y.-Y. Hu, M. Liu and H. Chen, *Journal of Power Sources*, 2018, **381**, 171-180.

73. A. Konarov, J. H. Jo, J. U. Choi, Z. Bakenov, H. Yashiro, J. Kim and S.-T. Myung, *Nano energy*, 2019, **59**, 197-206.

74. J. Qu, T. Sheng, Z.-g. Wu, T.-r. Chen, H. Chen, Z.-g. Yang, X.-d. Guo, J.-t. Li, B.-h. Zhong and X.-s. Dou, *Journal of Materials Chemistry A*, 2018, **6**, 13934-13942.

75. C. Julien, A. Mauger, A. Vijh and K. Zaghib, in *Lithium batteries*, Springer, 2016, pp. 29-68.

76. X. Yang, W. Tang, Q. Feng and K. Ooi, *Crystal growth & design*, 2003, **3**, 409-415.

77. R. Stoyanova, D. Carlier, M. Sendova-Vassileva, M. Yoncheva, E. Zhecheva, D. Nihtianova and C. Delmas, *Journal of Solid State Chemistry*, 2010, **183**, 1372-1379.

78. M. Yoncheva, R. Stoyanova, E. Zhecheva, E. Kuzmanova, M. Sendova-Vassileva, D. Nihtianova, D. Carlier, M. Guignard and C. Delmas, *Journal of Materials Chemistry*, 2012, **22**, 23418-23427.

79. S. Kumakura, Y. Tahara, S. Sato, K. Kubota and S. Komaba, *Chemistry of Materials*, 2017, **29**, 8958-8962.

80. R. J. Clément, P. G. Bruce and C. P. Grey, *Journal of The Electrochemical Society*, 2015, **162**, A2589.

81. R. Alcantara, P. Lavela, J. Tirado, E. Zhecheva and R. Stoyanova, *Journal of Solid State Electrochemistry*, 1999, **3**, 121-134.

82. Y. Li, X. Feng, S. Cui, Q. Shi, L. Mi and W. Chen, *CrystEngComm*, 2016, **18**, 3136-3141.